ORIGINAL PAPER

Fluid–structure interaction-based aerodynamic modeling for flight dynamics simulation of parafoil system

**Hong Zhu · Qinglin Sun · Xuefeng Liu ·
Jinglei Liu · Hao Sun · Wannan Wu ·
Panlong Tan · Zengqiang Chen**

Abstract Prediction of aerodynamic force is a crucial issue for parafoil canopy as the strong nonlinear fluid–structure interaction (FSI) between the flexible canopy material and flow field. Flight tests and wind tunnel experiments are difficult to analyze the aerodynamics of parafoil because of the limitation and difficulty of data measurement in an unknown environment. The objective of this study was to computationally derive the aerodynamic characteristics of parafoil, as an alternative to expensive and unrepeatable test regimes. Different from previous works that assume canopy structure as a rigid body and serve for the design of parafoil, this study focused on the precise dynamic modeling of parafoil based on FSI simulations. To investigate the aerodynamic performance of the full-scale canopy with stabilizers for better control, the strong coupling FSI simulations were performed using the incompressible computational fluid dynamics techniques. The highlight of this paper is to explore the effects of canopy inflation and trailing edge deflections on aerodynamic performance. Then the aerodynamic coefficients are identified by a linear regression method using the obtained database of high fidelity lift and drag forces. Furthermore, an accurate six-degree-of-freedom dynamic model of the parafoil system is implemented based on the estimated coefficients. Simulations are conducted to prove the dynamic stability of the model and the feasibility of trajectory tracking. At last, simulation results of basic motions are compared with airdrop testing data, which demonstrates that the established model is capable of accurately predicting the flight behaviors of the parafoil system.

Keywords Fluid–structure interaction · Parafoil system · Flexible deformation · Trailing edge deflection · Aerodynamic performance · Dynamic model

H. Zhu · Q. Sun (✉)· H. Sun · P. Tan · Q. Chen
College of Artificial Intelligence, Nankai University,
Tianjin 300350, China
e-mail: sunql@nankai.edu.cn

X. Liu · J. Liu
Beijing Institute of Space Mechanics & Electricity, Beijing
100094, China

X. Liu · J. Liu
Laboratory of Aerospace Entry, Descent and Landing
Technology, China Aerospace Science and Technology
Corporation, Beijing 100094, China

W. Wu
Institute of Mechanics, Chinese Academy of Sciences, Beijing
100190, China

1 Introduction

Compared to a round parachute, the parafoil has advanced maneuverability and gliding performance due to superior lift-to-drag ratio, therefore it has rapidly developed into a component of the aerodynamic deceleration system. A parafoil airdrop system consists of three parts: canopy, suspension ropes, and payload. The suspension ropes are connected between the lower surface of the canopy and payload. In the working process

of the parafoil system, it can be maneuvered to achieve turning motion by pulling a single steering line asymmetrically and deceleration by pulling down the right and left steering lines symmetrically. The pulling down of control lines, that is, the trailing edge (TE) deflection, will cause deformations of the canopy and lead to complex variations of aerodynamic forces of parafoil, thereby changes the flight direction and speed. The above characteristics make parafoil systems widely used in many fields, such as spacecraft recovery, military cargo airdrops, and civil jumping [1–3].

In order to improve the design and function of the parafoil system, a high fidelity dynamic model is needed to describe the behavior of the parafoil system in flight. The design of the control strategy of the parafoil airdrop system primarily depends on the prediction accuracy of aerodynamic characteristics, especially when the trailing edge deflects. But the estimation of the aerodynamics of parafoil is still not well solved. Owing to the complex fluid–structure interaction (FSI) between the parafoil canopy and surrounding flow field throughout the whole working process, the accurate modeling of the system is challenging. And it is difficult to predict the aerodynamic performance of the parafoil by theoretical analysis, numerical methods, and semiempirical methods [4].

Over the past few decades, much literature has studied the dynamic modeling of the parafoil system. Since 1975, Goodrick [5] established a longitudinal three degrees of freedom (DOF) dynamic model of the parafoil system and analyzed the stability in static and dynamic performance, which set off an upsurge in the modeling of the parafoil system. By analyzing the relative motions between the parafoil and the payload, the dynamic models of four DOF, six DOF, seven DOF, eight DOF, and higher DOF of parafoil system have been developed [6–9]. In these models, the calculation of the aerodynamic force adopted a geometrical fragmentation method, which cannot accurately predict the change of the overall aerodynamic performance of the canopy when the TE is deflected downward.

Due to the strong nonlinear and the time-varying coupling between the aerodynamic loads and the structure of the parafoil canopy, aerodynamic modeling is a bottleneck in the modeling of the parafoil system. In the previous studies, the prediction of aerodynamic forces utilized the lifting-line theory derived from fixed wings, regardless of the flexible deformation of the canopy and assuming that the aerodynamic shape of the parafoil

remains unchanged during flight. This assumption is basically reasonable in the steady gliding stage when the surrounding wind disturbance is small. Nevertheless, the lifting-line theory does not apply to the turning process, because the canopy deforms in both the span and chord directions, which affects the aerodynamic force distribution on the canopy obviously [10]. Recent researches [4,11–13] derived the aerodynamic coefficients for the rigid wing under different TE deflections without considering the flexibility of the canopy material. Based on the established computational aerodynamic model, flight dynamic simulations were carried out. However, keeping the canopy from complete inflation results in a lack of certainty for the effects that distortions might produce on the canopy surfaces and aerodynamic performance overall. Different from previous works that assumed canopy structures as rigid bodies and served for the design of parafoil, this study focused on the precise dynamic modeling of parafoil based on the FSI simulations.

Many different FSI strategies for the analysis of ram-air parachutes have been developed in recent years [14,15]. Benney et al. [16] proposed the first three dimensional (3-D) FSI simulation model for a large parafoil, which combined the deforming spatial domain stabilized space-time finite element algorithm with the Baldwin–Lomax turbulence model. However, this fully coupled method requires solving a large number of coupled nonlinear algebraic equations which results in high computational cost, so it is often impractical. Common methods used in the FSI numerical models are based on the partitioned method by solving the computational fluid dynamics (CFD) and computational structural dynamics (CSD) separately and sequentially [17], mainly in the hopes of solving the problem in a reasonable time with limited computer resources. In addition, many studies adopted loosely coupled methods for FSI simulations of the parafoil [18,19]. Fogell et al. simplified the parafoil model through an isolated cell (replacing a ram-air canopy) [20] and half of a semi-symmetrical parafoil wing with ribs as rigid material and fixed in space [21], assuming the shear modes in spanwise and chordwise directions were consistent. Moreover, Zhang Chun et al. [22] extended the research model to two kinds of 3-D full-scale parafoils with and without cells, respectively, and analyzed the characteristics of the flow field and structural deformations. However, it is obvious that, as shown in Fig. 1, not only will the ribs deform, the upper and lower surfaces of the

Fig. 1 Ram-air parachute side view during flight (Adapted from Airborne Systems, from https://airborne-sys.com/product/cargo-delivery-system-army-microfly-ii/)

canopy will also bulge outward (green arrows). Therefore, the cross section needs to be identified exactly in advance which brings difficulty to simulate the real shape of the canopy in flight.

Moreover, few studies made improvements to reduce the influences of model oversimplification and imposed boundary conditions. Takizawa et al. [23] enhanced the FSI model by adding suspension ropes and stabilizers to obtain the initial shape and initial loads acting on the parafoil. The study in [24] gave an investigation of closely coupled FSI simulation results about the deformation of MC-4 ram-air parachute, using the technology of control line retraction with prescribed pressure distributions embedded in the finite element code LS-DYNA. The constraints added in this way make the deformation of the canopy more realistic. Above efforts on the FSI simulations of the parafoil system brought us a deeper insight into the interaction between structural mechanics and fluid dynamics of the canopy and confirmed the differences in the aerodynamic performance between the initial cut pattern and the flying shape of a parafoil.

Recent studies have shown that the incompressible computational fluid dynamics techniques of LS-DYNA is a practical tool for precisely modeling FSI problems [25–28], which can exchange information between the fluid and structure domains automatically to promote the solution efficiency. Previous FSI coupling simulations of parafoil mainly focused on the steady gliding stage, assuming that the geometrical model is symmetrical. In this paper, we concentrate on the asymmetric response of the flow field and the aerodynamics of the parafoil during the turning motion caused by the steering of control lines. The purpose of this paper

was to establish an accurate aerodynamic model for the flight tests of the parafoil system based on the strongly coupled FSI method. The FSI simulations were performed using CFD techniques combined with the LS-DYNA solver, considering the material properties of the parafoil, and aerodynamic forces and deformations of a full-scale 3-D canopy under various TE deflections and angles of attack were analyzed. Based on the aerodynamic data, we established a detailed aerodynamic model database and further built an accurate six-DOF dynamic model for the parafoil airdrop system. Finally, we conducted airdrop tests to verify the effectiveness and feasibility of the proposed methods.

The remainder of the paper is organized as follows. Section 2 provides a brief description of a six-DOF dynamic model of parafoil system. Section 3 details the FSI numerical models. FSI simulation results and analysis are presented in Sect. 4. Dynamic simulations and stability analysis in normal mode and perturbations in Sect. 5 and airdrop test results in Sect. 6 verify the validity of the developed model. Section 7 concludes the study.

2 Dynamic model of parafoil system

To improve the design and functionality of the parafoil system, establishing a realistic dynamic model is important to represent the behavior and predict the motion of the parafoil system in flight. Figure 2 shows the parafoil system in steady gliding. The angle between the freestream velocity V_∞ and the lower surface of the canopy is the angle of attack, denoted by α. The aerodynamic force acting on the parafoil F_{aero} is decomposed into drag $\mathbf{D}_c$ and lift $\mathbf{L}_c$ along the opposite direction of motion and its vertical direction. The other two forces acting on the system are the gravity $m_c g$ acting on the centroid of the canopy and the gravity $m_p g$ acting on the centroid of payload, respectively.

2.1 Motion equations

In this paper, a six-DOF model is used to simulate the overall movement of the parafoil system, including three degrees of freedom for inertial position and three degrees of freedom for orientation of the mass center. According to the Kirchhoff equations of motion [8], the six-DOF equations of motion including the appar-
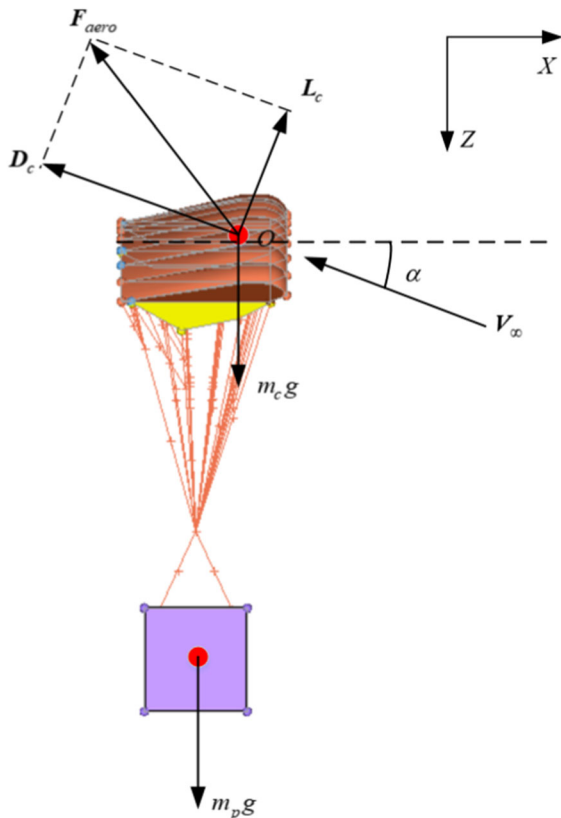
Fig. 2 Schematic of parafoil system in steady flight

ent mass of parafoil [29] can be expressed in matrix forms as follows:

$$\begin{bmatrix} \dot{v} \\ \dot{w} \end{bmatrix} = \begin{bmatrix} J_{11} & J_{12} \\ J_{21} & J_{22} \end{bmatrix}^{-1} \begin{bmatrix} F \\ M \end{bmatrix} \tag{1}$$

$$F = F_{aero}^s + F_{aero}^p + F_G + F_{ex}^a + F_{ex}^r \tag{2}$$

$$M = M_{aero}^s + M_{aero}^p + M_{ex}^a + M_{ex}^r \tag{3}$$

$$J_{11} = m_a + m_r \tag{4}$$

$$J_{22} = I_r + I_a - L_{op}^\times m_a L_{op}^\times \tag{5}$$

$$J_{12} = -J_{21}^T = -m_a L_{op}^\times \tag{6}$$

here $\dot{v}$ and $\dot{w}$ are the acceleration and angular acceleration of the parafoil system, respectively. F and M are the applied forces and moments, respectively. J_{11} denotes the sum of real mass and apparent mass of the system, J_{22} denotes the rotational inertia of real mass and apparent mass. J_{12} and J_{21} are coupling terms. The total forces acting on the parafoil system includes aerodynamic forces of canopy F_{aero}^s and payload F_{aero}^p, gravity of the system F_G, coupling forces of apparent mass F_{ex}^a and real mass F_{ex}^r. M_{aero}^s, M_{aero}^p, M_{ex}^a,

M_{ex}^r represent the moments of corresponding forces, respectively. $L_{op}^\times$ denote the three by three transition matrix from mass center O to added mass center P.

The aerodynamic forces acting on the parafoil have a great influence on the movement of the parafoil system, which is composed of lift $\mathbf{L}_c$ and drag $\mathbf{D}_c$ of the parafoil, and their expressions can be written as follows:

$$\mathbf{L}_c = \frac{1}{2}\rho V^2 S C_L \tag{7}$$

$$\mathbf{D}_c = \frac{1}{2}\rho V^2 S C_D \tag{8}$$

where ρ is the density of air, V is the freestream velocity, S is the area of the canopy, C_L and C_D are the lift and drag coefficients, respectively.

Although obtaining high-fidelity lift and drag coefficients of parafoil is essential, there is still no general method owing to the aerodynamic characteristics of parafoil vary with the airfoil and configuration. Taking into consideration the additional aerodynamic forces induced by the TE deflection, the aerodynamic model parameters are expressed as follows:

$$C_L = C_{L0} + C_{L\alpha}\alpha + C_{L\delta}\delta \tag{9}$$

$$C_D = C_{D0} + C_{D\alpha}\alpha + C_{D\delta}\delta \tag{10}$$

where α denotes angles of attack, $\delta \in [0, 100\%]$ is TE deflection. C_L and C_D denote lift and drag coefficients, respectively, C_{L0} and C_{D0} represent their values at zero angle of attack, respectively, $C_{L\alpha}$ and $C_{D\alpha}$ are the slopes of lift and drag curves, respectively. Due to the nonlinear relationship between the TE deflection coefficients $C_{L\delta}$, $C_{D\delta}$ and the angles of attack α [30,31], we introduced the following second-order relation model:

$$C_{L\delta} = C_{L\delta 0} + C_{L\delta\alpha}\alpha + C_{L\delta\alpha^2}\alpha^2 \tag{11}$$

$$C_{D\delta} = C_{D\delta 0} + C_{D\delta\alpha}\alpha + C_{D\delta\alpha^2}\alpha^2 \tag{12}$$

where $C_{L\delta 0}$, $C_{L\delta\alpha}$, $C_{L\delta\alpha^2}$, $C_{D\delta 0}$, $C_{D\delta\alpha}$, $C_{D\delta\alpha^2}$ are the deflection coefficients to be identified.

2.2 Identification of aerodynamic coefficients

The FSI technique is adopted to solve the aerodynamic forces of the canopy during trailing edge deflecting and provide a database for the identification of the aerodynamic model.

Replacing Eqs. (11), (12) into (9), (10), respectively, the unknown parameters can be identified by linear regression method (LRM). We write above aerodynamic model as matrix form of the linear regression

model as follows:

$$y = X\theta \tag{13}$$

where θ denotes the vector of unknown parameters to be identified, X is the matrix of input variables (i.e., α, δ), y denotes output vector obtained from FSI simulation results. The angles of attack varies from $0°$ to $20°$ with an interval of $2°$, and the variable values of the percentage of TE deflection δ in full braking are 0%, 10%, 40%, 70%, 100%. The unknown parameters can be estimated as

$$\theta = \left(X^{\mathrm{T}}X\right)^{-1} X^{\mathrm{T}}y \tag{14}$$

3 Computational model and numerical method

To accurately capture the FSI phenomenon, it is essential to couple the fluid solver and structural solver running at the same time. By using the strong FSI coupling capabilities of LS-DYNA, the CFD solver and its structural mechanic solver are combined to carry out the simulation, which greatly improves solving efficiency.

Two sets of simulation experiments were carried out to investigate the influence of structural deformations on the aerodynamics of the parafoil canopy. One set used the CFD method to calculate the aerodynamic forces considering the canopy as a rigid body, and the other set used the FSI coupling method taking into account the flexibility of canopy material.

3.1 Computational model

3.1.1 Structural modeling

The structural model for FSI simulations was adopted from the parafoil used in airdrop tests conducted by our research group. The basic computer aided design (CAD) model of parafoil with 15 cells was created by SOLIDWORKS, as represented in Fig. 3. The parafoil was composed of three parts: canopy, stabilizers, and suspension ropes. Figure 3a shows the initial undeformed configuration of the parafoil, where the two red lines connected to the trailing edge represent the control ropes. The pulling down of the control rope on each side causes the trailing edge of the corresponding side to deflect. The left steering lines adhered to the trailing
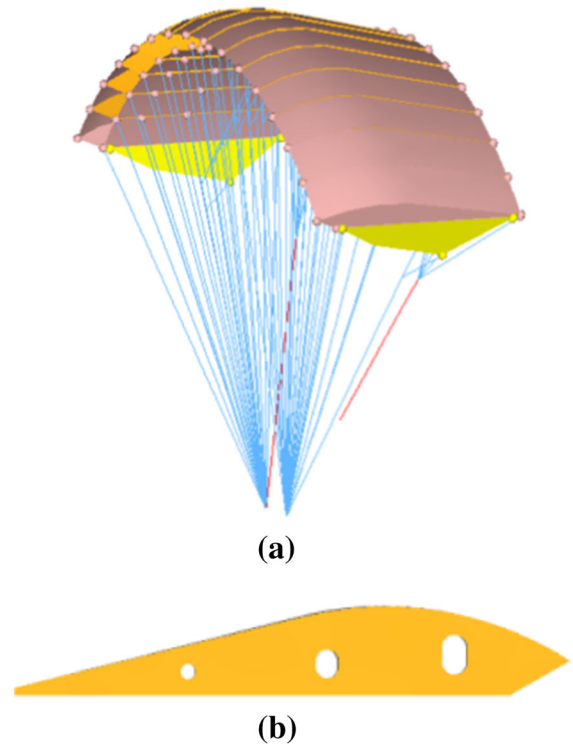
(a)

(b)

Fig. 3 Initial parafoil model. **a** CAD model of the full-scale geometry. **b** A rib

edge have not yet been gathered to the intersection of suspension lines. A rib with several apertures to balance the air pressure between two adjacent cells as shown in Fig. 3b.

The dimension parameters of the airfoil section and canopy can refer to Table 1. The parafoil has a rectangular planform and two stabilizers attached to the end cells. The material of the canopy was made from fabric, which was modeled as membrane. The suspension lines were modeled as cables. The specific material properties of the canopy fabric and suspension lines are shown in Table 2.

The finite element model of the undeformed configuration is shown in Fig. 4. The discretization of the canopy used quadrilateral elements, and the ribs were divided into triangle elements. The confluence points at one end of the ropes were fixed to constrain the canopy. The precise setup of the cable model can reduce the original error from the applied constraints.

Table 1 Dimension parameters of the parafoil

Parameter	Value
Chord length (m)	3.18
Span length (m)	10.5
Aspect ratio	3.3
Leading inlet length (m)	0.36
Leading inlet angle (°)	135
Relative thickness	0.12
Average rope length (m)	6.8

Table 2 Material properties

Item	Membrane	Cable
Young's modulus (Pa)	4.309×10^8	9.7×10^{10}
Density (kg/m^3)	533.77	462
Poisson's ratio	0.14	–
Thickness (m)	1×10^{-4}	–
Cross-sectional area (m^2)	–	4.91×10^{-6}
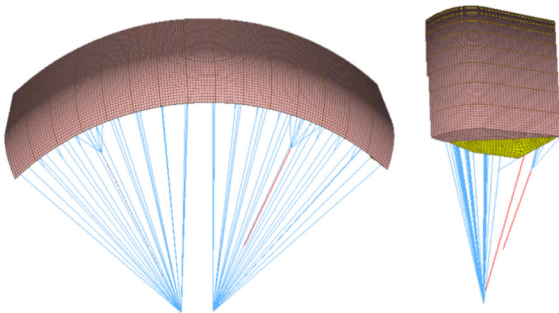
Fig. 4 Underformed mesh model. Front (left) and side (right) views

3.1.2 Fluid modeling

The simulations at different angles of attack ranging from 0° to 20° were conducted. The air was considered as incompressible with a density of 1.225 kg/m^3 and the reference value of pressure was 101,325 Pa. The flow rate was identical to the glide speed of 10 m/s. The boundary conditions of the fluid domain consist of an inflow boundary with a constant velocity, a zero-pressure outflow boundary, and free slip boundary conditions on the side walls. The surfaces of the parafoil were applied as the non-slip boundary.

The fluid domain size is shown graphically in Fig. 5. According to the CFD simulation experiments in ref-
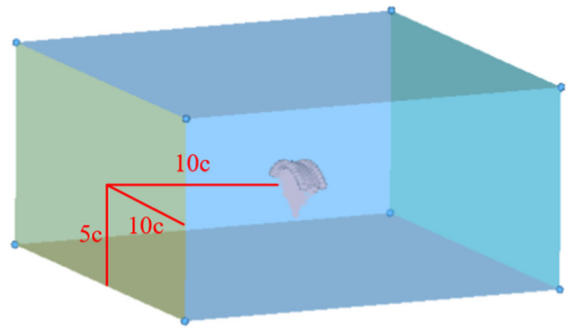
Fig. 5 Relative dimension of fluid domain
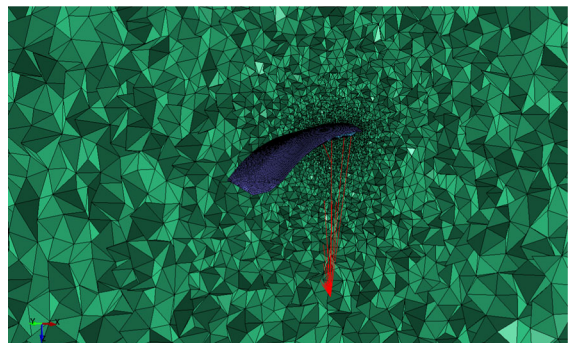
Fig. 6 Fluid mesh near the canopy

erence [32,33], the distances from the fluid domain boundaries to the parafoil model were set as 10c, 5c, 10c, respectively. The parafoil mesh model was located at the center of the fluid domain. The surface of the canopy and fluid boundaries were discretized by triangular shell elements. The volume mesh was generated automatically by the meshing capabilities of the LS-DYNA preprocessor. The geometric boundaries of the fluid domain and the structural domain must coincide, but the meshes do not have to match. Figure 6 displays a mesh view near the canopy. The size of the first layer of boundary mesh close to the canopy was determined to around 1 mm and the growth rate of the boundary mesh away from the canopy was 1.1 based on the requirements of the selected turbulence model for the boundary layer mesh [12]. The final computational model has 1,010,000 meshes after the verification of grid independence, which is accurate enough for turbulence computations. The Spalart-Allmaras (SA) was selected as the turbulence model. It is applicable to solve turbulent viscosity for aerospace problems and shows good results in circumstances of wall-bounded flows and adverse pressure gradients [34].

3.2 Mathematical representation of fluid–structure interaction

Let Ω_f and Ω_s be the spatial domain of fluid and structure, respectively. And they interact at the common boundary Γ where the canopy is at any time $t \in (0, T)$. The governing equations for the fluid–structure interactions are as follows.

3.2.1 Governing equations of structural mechanics

The deformations of the canopy fabric are governed by the nonlinear dynamic characteristics of the membrane material under external forces from flow pressure and shear stress. The governing equations for the structural mechanics derived from the conservation of linear momentum are written as follows:

$$\rho_s \left(\frac{d^2 \boldsymbol{x}}{dt^2} - \boldsymbol{f}_s \right) - \nabla \cdot \boldsymbol{\sigma}_s = 0 \quad \text{in} \quad \Omega_s \tag{15}$$

where ρ_s is the material density, $\boldsymbol{x}$ is the displacement vector, $\boldsymbol{f}_s$ is the external forces, and $\boldsymbol{\sigma}_s$ is the Cauchy stress tensor.

3.2.2 Governing equations of fluid mechanics

The Navier–Stokes equations for incompressible Newtonian fluid can be written as:

$$\rho_f \left(\frac{\partial \boldsymbol{u}}{\partial t} + \boldsymbol{u} \cdot \nabla \boldsymbol{u} - \boldsymbol{f}_f \right) - \nabla \cdot \boldsymbol{\sigma}_f = 0 \quad \text{in} \quad \Omega_f \tag{16}$$

$$\nabla \cdot \boldsymbol{u} = 0 \quad \text{in} \quad \Omega_f \tag{17}$$

where ρ_f, $\boldsymbol{u}$, $\boldsymbol{f}_f$ denote fluid density, velocity and the external forces, respectively. The stress tensor $\boldsymbol{\sigma}_f$ is defined as:

$$\boldsymbol{\sigma}_f = -p\mathbf{I} + \mu(\nabla \boldsymbol{u} + \nabla \boldsymbol{u}^{\mathrm{T}}) \tag{18}$$

here p, $\mathbf{I}$, and μ are fluid pressure, identity tensor, and the dynamic viscosity, respectively. Proper boundary conditions and initial conditions are needed for the solution of the above dynamic equations. The boundary conditions can be defined as

$$\boldsymbol{u} = \boldsymbol{v} \quad \text{on} \quad \Gamma \tag{19}$$

where $\boldsymbol{v}$ is the given function that is imposed on the boundary. The initial condition is the specified divergence-free velocity field.

A projection method is used by the CFD solver for the time integration of Navier–Stokes equations [35], which decouples the pressure and velocity of the fluid. In this way, three equations for momentum and one equation for solving incompressibility constraints are obtained. The three-step fractional method is adopted to calculate the velocity, and the specific forms can refer to [36].

The SA model mentioned in Section 3.1.2 is used to calculate turbulence, and the specific forms of the control equations are

$$G_v + \frac{1}{\sigma_{\tilde{v}}} \left[\frac{\partial}{\partial x_j} \left\{ (\mu + \rho \tilde{v}) \frac{\partial \tilde{v}}{\partial x_j} \right\} + C_{b2} \rho \left(\frac{\partial \tilde{v}}{\partial x_j} \right)^2 \right]$$
$$- Y_v + S_{\tilde{v}} = \frac{\partial}{\partial t} \rho \tilde{v} + \frac{\partial}{\partial x_k} (\rho \tilde{v} u_k) \tag{20}$$

where $G_v = G_{b1} \rho \tilde{S} \tilde{v}$ is the generation item,

$$Y_v = C_{w1} \rho f_w \left(\frac{\tilde{v}}{d} \right)^2 \tag{21}$$

$$\tilde{S} \equiv \frac{\tilde{v}}{\kappa^2 d^2} \left(1 - \frac{\chi}{1 + \chi \left(\frac{\chi^3}{\chi^3 + C_{v1}^3} \right)} \right)$$
$$+ \sqrt{\frac{1}{2} \left(\frac{\partial u_k}{\partial x_j} - \frac{\partial u_j}{\partial x_k} \right)} \tag{22}$$

$$\chi = \frac{\tilde{v}}{v} \tag{23}$$

$$C_{w1} = \frac{C_{b1}}{\kappa^2} + \frac{(1 + C_{b2})}{\sigma_{\tilde{v}}} \tag{24}$$

$$f_w = f_{w1} f_{w2} \tag{25}$$

$$f_{w1} = \left(\frac{\tilde{v}}{\tilde{S} \kappa^2 d^2} + C_{w2} \left(\left(\frac{\tilde{v}}{\tilde{S} \kappa^2 d^2} \right)^6 - \frac{\tilde{v}}{\tilde{S} \kappa^2 d^2} \right) \right) \tag{26}$$

$$f_{w2} = \left(\frac{1 + C_{w3}^6}{\left(\frac{\tilde{v}}{\tilde{S} \kappa^2 d^2} + C_{w2} \left(\left(\frac{\tilde{v}}{\tilde{S} \kappa^2 d^2} \right)^6 - \frac{\tilde{v}}{\tilde{S} \kappa^2 d^2} \right) \right)^6 + C_{w3}^6} \right)^{\frac{1}{6}} \tag{27}$$

where $C_{b1} = 0.1355$, $C_{b2} = 0.622$, $\kappa = 0.4187$, $\sigma_{\tilde{v}} = 2/3$, $C_{w2} = 0.3$, $C_{w3} = 2$, and d represents the distance from the wall.

In general, some non-dimensional variables are introduced based on the wall shear stress:

$$U^+ = \frac{U}{u_\tau} \tag{28}$$

$$y^+ = \frac{\Delta y u_\tau}{\upsilon} \tag{29}$$

$$u_\tau = \sqrt{\frac{\tau_w}{\rho_f}} \tag{30}$$

where U^+ and y^+ are the dimensionless velocity and distance from the wall, respectively. U is the velocity at a distance Δy from the wall in the direction parallel to the wall, u_τ is the friction velocity, υ is the dynamic viscosity of the fluid, τ_w is the wall shear stress.

The near-wall zone can be divided into three sublayers:

(1) Viscous sublayer: it is a thin layer close to the wall, in which the viscous force plays a leading role compared with the turbulent shear stress. Thus the flow behavior is similar to laminar motion, and the velocity component parallel to the wall is linearly distributed along the normal direction of the wall. In this region, $y^+ < 5$.

(2) Transition layer: it is located outside the viscous layer, where the effect of viscous force is equivalent to turbulent shear stress, and the fluid is a mixture of turbulence and laminar flow. Due to the extremely thin thickness of the transition layer, it is usually classified into the logarithmic layer. In the transition layer, y^+ is between the range of $5 \sim 60$.

(3) Logarithmic layer: it is the outermost layer of the near-wall zone. The turbulent shear stress plays a dominant role, so the flow is in a fully developed turbulent state and the velocity distribution is close to logarithmic law. In this region, $y^+ > 60$.

The wall function method uses semiempirical formulas to calculate the near-wall kinematic viscosity υ to ensure that the solutions of the wall shear stress are correct. The real velocity normal to the wall is given by a general function:

$$U^+ = f(y^+) \tag{31}$$

Wall functions are used to modify the kinematic viscosity to obtain the effective wall viscosity:

$$\upsilon_w = \upsilon \left(\frac{y^+}{f(y^+)} \right) \tag{32}$$

The standard wall functions provide the necessary wall boundary conditions by using the logarithmic correction method and allows the use of relatively coarse grids in the near-wall region for the case of high Reynolds number $(Re > 10e^6)$.

$$U^+ = f(y^+) = \begin{cases} y^+, & y+ < 11.25 \\ \frac{1}{\kappa} log(Ey^+), & y^+ > 11.25 \end{cases} \tag{33}$$

where κ is the Karman constant and E is the constant related to surface roughness.

The enhanced wall function uses a continuous function that is valid for all y^+ to achieve a smooth blend between the viscous sublayer and the logarithmic layer:

$$\begin{cases} f(y^+) = e^\Gamma u_{lam}^+ + e^{\frac{1}{\Gamma}} u_{turb}^+ \\ \Gamma = \frac{-0.01(y^+)^4}{1+5y^+} \end{cases} \tag{34}$$

where e^Γ and $e^{\frac{1}{\Gamma}}$ are the blending functions, $u_{lam}^+ = y^+$ and $u_{turb}^+ = \frac{1}{\kappa} log(Ey^+)$ are the general viscous sublayer and log-law region profiles.

3.2.3 Fluid–structure interaction framework

In order to solve the fluid–structure coupling problem accurately, the fluid domain and the structure domain must be combined to solve simultaneously. The forces acting on the canopy and the influence of canopy deformation on the fluid must be calculated in each time step. CFD solver can not only be used as a single fluid solver but also can be loosely coupled or strongly coupled with the structural solver to solve fluid–structure coupling problems. In each time step, the loose coupling strategy only needs to solve the convection domain and the structural domain once, but the strong coupling method solves the convection domain and structural domain many times in each time step until the variables on the fluid–structure coupling interface reach the convergence condition, and then the next cycle is carried out. We use the strong coupling strategy to solve the problem for the reason that it is the most accurate method to solve the transfer load and displacement in the strong nonlinear problem. LS-DYNA uses the implicit solver to solve structural mechanics in strong coupling analysis.

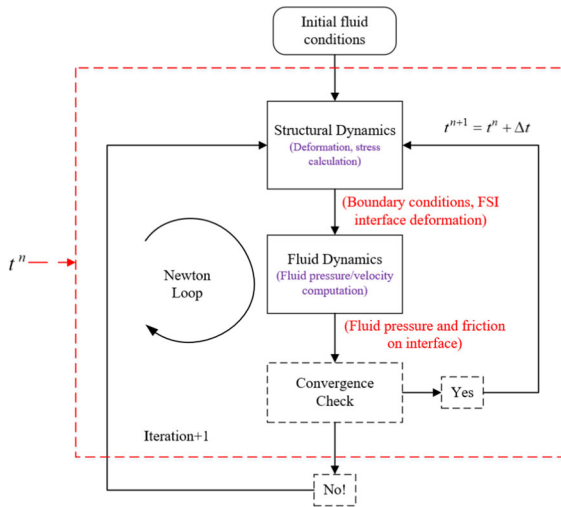Figure 7 shows the flowchart of the FSI solution. The pressure loads applied on the structure and the con-

Fig. 7 Flowchart of FSI solution

Table 3 Grid independence examination

Mesh model	Number of grids	Number of nodes	C_L	C_D
A	492154	119025	0.89	0.28
B	1394220	341088	0.78	0.09
C	1919376	432397	0.64	0.15
D	3510539	669203	0.63	0.14

sequent displacement are transferred iteratively across the FSI interface, i.e., the canopy boundary, until the variables of both domains reach an equilibrium. Compared to the loosely coupled scheme, which requires only one solution in two separate software by a sequential manner at each time step, this is an efficient and accurate method. With the more closely coupled manner, not only the chief effects but also secondary deformations of the canopy material can be captured. Accordingly, the lift and drag forces can be modified more precisely.

4 Fluid–structure interaction simulation and analysis

For reference purposes, the initial nominal parafoil model as shown in Fig. 3 with geometrical parameters given in Table 1 was taken as a basis. Firstly, the parafoil was assumed as rigid without considering the structural deformation, so only the flow field loads were solved. Then, the FSI coupling simulations were conducted with the material parameters of the structure given in Table 2. Finally, the aerodynamic performances were discussed taking into account the influence of inflation and different TE deflections on the canopy deformations, and aerodynamic forces under the full range of angles of attack were estimated.

To predict the motion of the parafoil payload system, it is necessary to understand its aerodynamic characteristics. The LS-DYNA software version R10 was used

to realize the FSI simulations of the parafoil system. Due to high-performance MPP scalability, the finite element model was implemented in a workstation with a high number of CPUs. After aerodynamic stabilization of the parafoil, several flap deflections were computed within 2s. The aerodynamic forces were taken as the steady-state values after each canopy deformations reach stability.

4.1 Validation of FSI simulation

4.1.1 Mesh independence validation

In order to determine the independence of the grid, we use four different sizes of mesh models to calculate the lift and drag coefficients of parafoil at the angle of attack of 0°. The results are shown in Table 3. Among the four mesh models, the lift coefficient error between Model C and Model D is only 1.6%, which indicates that Model C has reached the acceptable accuracy of the current numerical simulation. Therefore, the grid sizes of Model C are used as the standard parameters for further research.

4.1.2 Wind tunnel test validation

The simulation results of NASA's Model 12 were compared with the wind tunnel experimental data available in [37] to verify the CFD solver and the selected turbulence model, as shown in Fig. 8. The comparison results show that the lift and drag coefficients of simulations match the experimental data well at all angles of attack, and the maximum error does not exceed 8%, which occurs after the stall. These results give us confidence in using numerical simulation methods to predict the aerodynamic forces of the parafoil in this article.
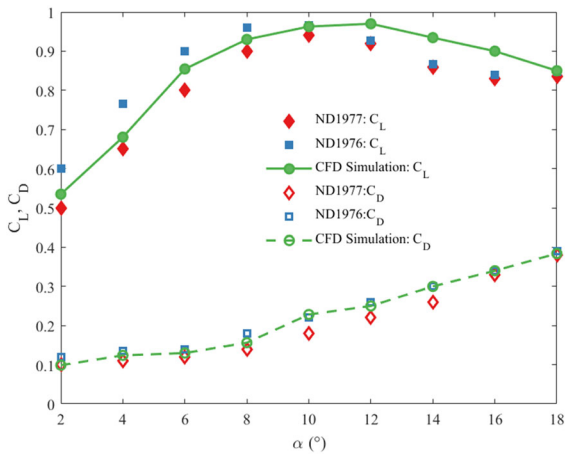
Fig. 8 Comparison of wind tunnel test with simulation

(a)

(b)

Fig. 9 Comparison of canopy structure between **a** nominal shape of parafoil and **b** an inflated one

4.2 Structural deformation of parafoil canopy

In comparison to an "ideal" rigid canopy model with designed dimensions, the FSI model can simulate the inflated shape of the canopy more realistically, and describe the change of shape quantitatively in the spanwise and chordwise directions, as well as the anhedral-arc radius and projection planform.

Figure 9 presents a comparison of the nominal rigid canopy model to the inflated FSI model results. The top view shows the differences of the planform shapes before and after inflating. It is apparent that inflation caused an effective reduction in spanwise end cells and chordwise direction of the canopy. The front view shows that the bulge of cells caused the fluctuations of upper and lower wing surfaces, and the leading area at the middle cell exhibited a visible concave impression due to the pressure of bypass flow from the inlet. Besides, the deformations of stabilizers and ribs made them no longer lie in a plane parallel to the chordwise. These observations are consistent with the phenomenon noticed in Fig. 1.

Table 4 shows detailed comparisons of parameters between the nominal parafoil model and the flexible inflated parafoil model. Obviously, the size of parafoil shrank in both spanwise and chordwise directions because of inflating. The projected area and span length were reduced the most, by 5.34% and 3.47% respectively, indicating that the designed initial nominal parafoil model was somewhat close to the real dimensions of the inflated model.
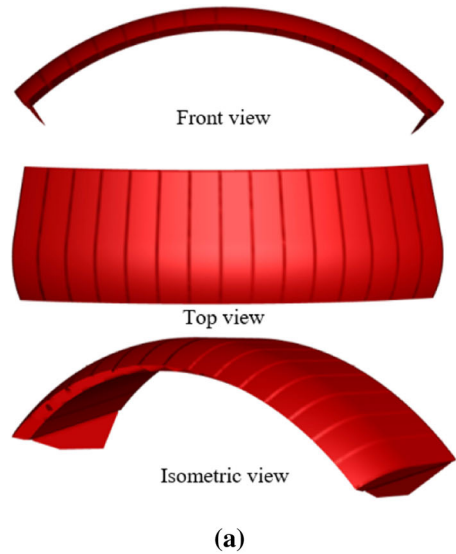
In addition, The FSI method was used to simulate the deformations of the canopy when the left control ropes pulling down by 10%, 40%, 70%, and 100% respectively (as shown in Fig. 10). From Fig. 10, we can see that as the pull-down amount of the control rope increases, the deformation of the canopy becomes larger and larger, and it primarily occurs on one-third of the canopy from the trailing edge at the left side.

Table 4 Relative shrinkage for the inflated parafoil canopy

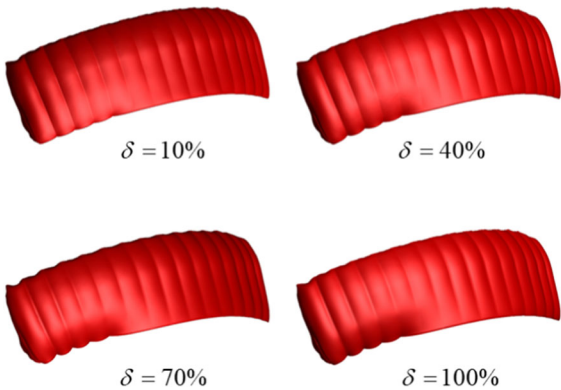| Models	Span (m)	Chord (m)	Area (m^2)	Aspect ratio
Initial geometry	7.033	2.257	16.628	3.116
Inflated canopy	6.789	2.227	15.740	3.049
Relative shrinkage	3.47%	1.33%	5.34%	2.17%

Fig. 10 Parafoil deformations with unilateral deflection

4.3 Flow field simulation analysis

One of the main 3-D effects is the vortex sheet leaving the rear edge of the canopy and the tip vortexes formed at the end-cells that are no longer parallel to the free stream direction (as shown in Fig. 11a). Fig. 11b shows the flow streamlines through the upper surface convergence downstream to some extent while slightly divergence through the lower surface. After flowing over "undulant" surfaces of the inflated canopy, the fluid is no longer explicitly parallel to the ribs, causing a velocity component along the span direction, which reduces the effective airspeed. This phenomenon is difficult to observe from a single-cell canopy model with symmetrical boundaries [21].

The flow field simulation results between the rigid canopy model and the flexible inflated canopy model were compared, for a rectangular planform 15-cell parafoil with an aspect ratio of 3.3, as shown in Fig. 12. The aerodynamic performances of the two models have little difference at low angles of attack, but the difference gradually increases under the high angle of attack. Besides, the results indicate that the flexible model has a larger stall angle of attack and a greater maximum lift coefficient than the rigid model.
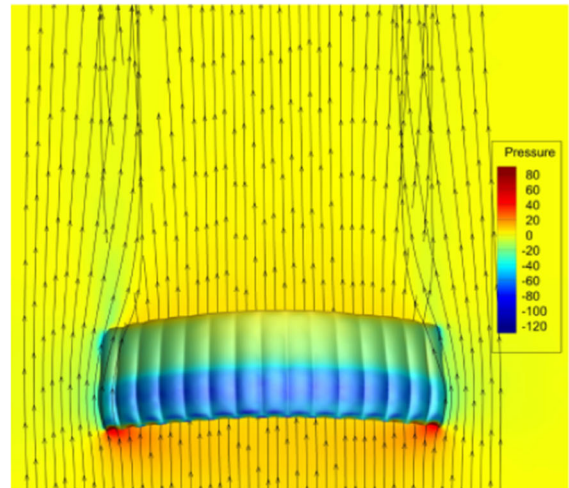
(a)
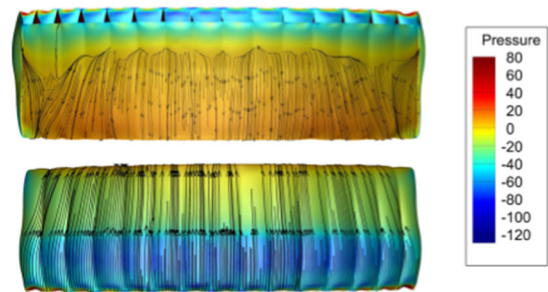
(b)

Fig. 11 Streamlines flowing over the inflated canopy and pressure contours. **a** Along chord direction. **b** Over upper and lower surfaces

From Fig. 12b, the lift to drag ratio of the rigid model is bigger than that of the flexible model under $\alpha = 6°$. As the angle of attack increases, the L/D of the flexible model becomes larger. The maximum L/D of the rigid model is 5.7 at $\alpha = 6°$, while the maximum L/D of the flexible model is 5.9 at $\alpha = 8°$. This could be attributed to the reduced of the chord length and span length caused by the inflation of the canopy. The detailed geometrical parameters are shown
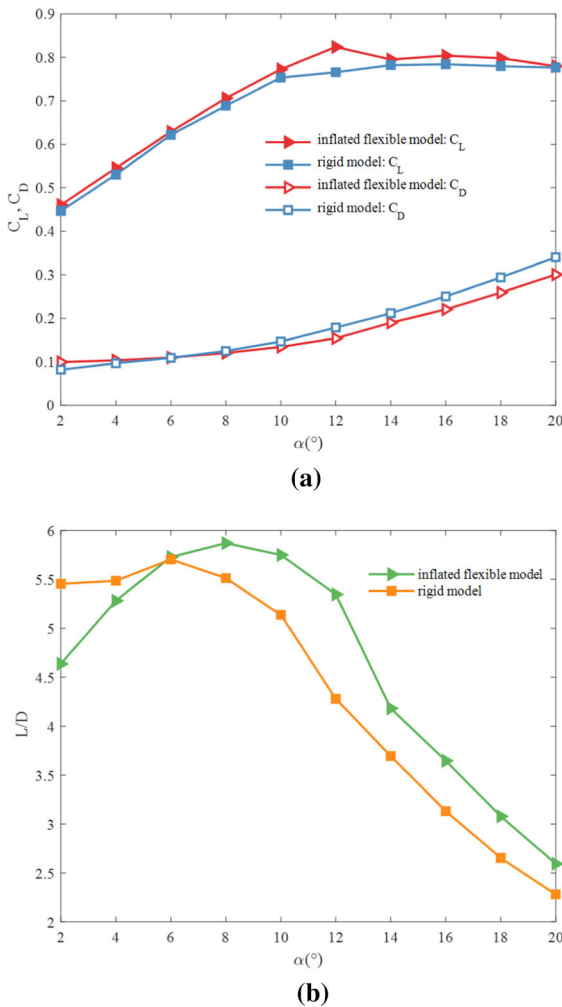
(a)

(b)

Fig. 12 Comparison of aerodynamic coefficients between rigid model and inflated flexible model. **a** Lift and drag coefficients. **b** Lift to drag ratio

in Table 4. In addition, inflation also causes changes in the size of the leading edge incision. These geometric changes all contributed to the discrepancy of the aerodynamic performance between the rigid model and the inflated flexible model [38]. As a result, the nominal parafoil model underestimates the aerodynamic performance compared with the flexible model. Through the comparisons in Fig. 12, we can know the influence of inflated shape on aerodynamic performance increases as the angle of attack.

The pressure distributions of the inflated model with angles of attack change from 4° to 14° are displayed in Fig. 13. From the comparison of the pressure profiles on the upper surfaces, we can notice that with the

increment of angles of attack, the low-pressure region grows gradually and moves towards the leading edge until $\alpha = 12°$ when the air flows through the middle cells begin to separate in advance. This can be demonstrated from Fig. 12a that the parafoil approaches stall at $\alpha = 12°$ and has entered the stall zone at $\alpha = 14°$. It is explained by the pressure distribution in Fig. 13f, where the flow separation at the middle leading edge area is obvious and the downstream flows are no longer reattached, indicating that the parafoil has reached the stall.

The main reason for the separation is that the inlet incision causes the flow at the leading edge and TE of the upper surface to separate at the same time, and the pressure gradient near the leading edge incision is very large. Besides, the flow velocity inside the cells is close to stagnation which becomes the driving force for the parafoil to maintain its inflated shape. To further verify, Fig 14a and b present the 3-D streamlines and pressure distribution on the outer surfaces of the inflated flexible canopy at angles of attack of 12° and 14°, respectively. Comparing the two figures, we can know that a large area vortex in the center cells of parafoil causes stall.

Similar to ordinary wings, the pressure on the lower surface of the parafoil is higher than that on the upper surface, and upward turbulence will occur at the wingtips, thus forming wingtip vortex cores. However, due to the streamline changes at end-cells of the parafoil, the effective angle of attack is reduced relative to the middle of the parachute makes the flow at wingtips do not severely separate at high angles of attack. This phenomenon is consistent with the experimental observation in the literature [39].

Figure 15 shows the vorticity plots at the spanwise central sections of the canopy and the corresponding pressure coefficient (Cp) curves on the outer surface to illustrate the flow characteristics of the parafoil.

As shown in Fig. 15, the boundary layer on the upper surface gradually increases after the flow passing through the thickest point in the chord direction when moving towards the trailing edge, corresponding to a separation zone. On the other hand, the flow is separated obviously at the beginning of the leading edge on the bottom surface, and it returns to an attached flow at half of the distance from the trailing edge.

The vorticity magnitude contour in Fig. 15b confirms that the boundary layer thickness of the upper surface at $\alpha = 12°$ is greater than that at $\alpha = 8°$, which corresponds to the earlier flow separation. On
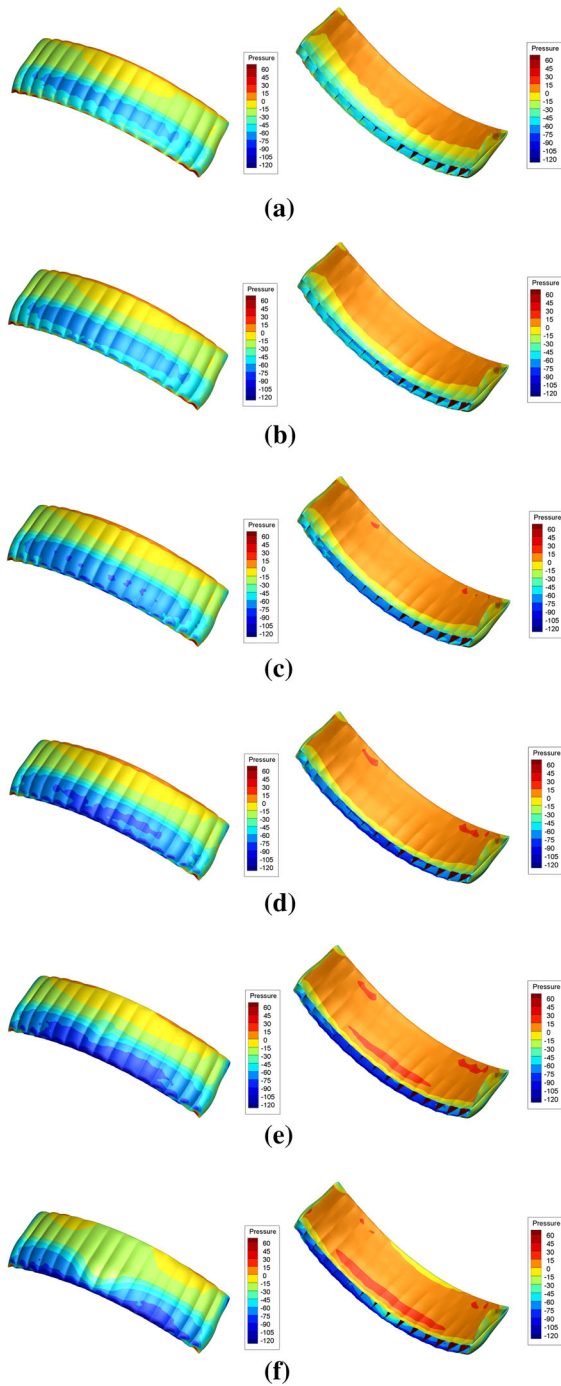
Fig. 13 Upper (left) and lower (right) surfaces pressure distribution of inflated parafoil at **a** $\alpha = 4°$. **b** $\alpha = 6°$. **c** $\alpha = 8°$. **d** $\alpha = 10°$. **e** $\alpha = 12°$. **f** $\alpha = 14°$

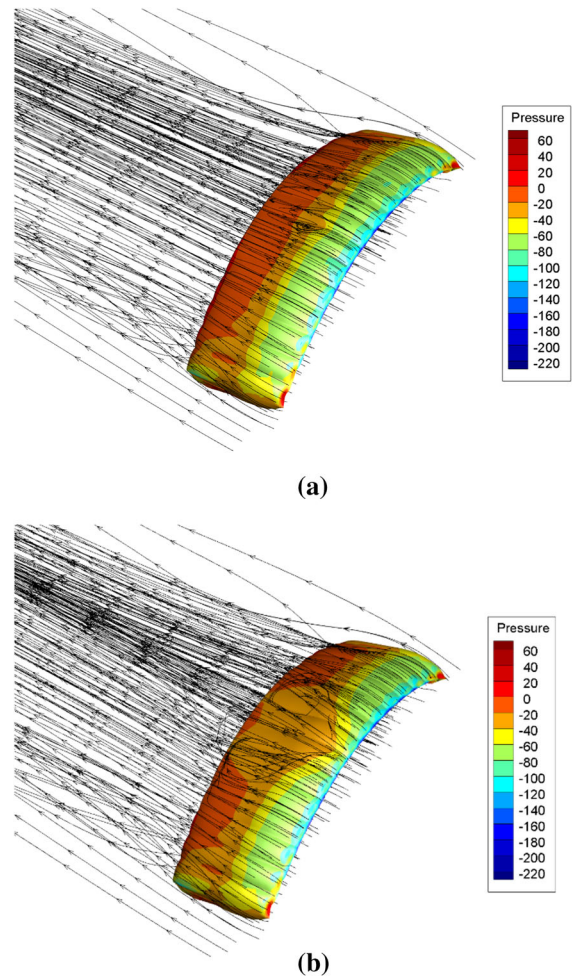**Fig. 14** 3-D streamlines and pressure contour on the canopy at **a** $\alpha = 12°$. **b** $\alpha = 14°$

the contrary, the thickness of the boundary layer on the lower surface becomes smaller, indicating that the separated flow is less than that at $\alpha = 8°$. It seems that the decrease of the boundary layer thickness at the lower surface is more obvious than the increase of thickness at the upper surface, which indicates that a larger attack of angle can achieve higher parafoil performance.

The increase of boundary layer thickness in Fig. 15a starts when the flow from the inlet face intersects with the fluid on the upper surface, thereby changing the direction to bypass the sharp leading edge. This phenomenon is verified by the local maximum of boundary layer thickness at the leading edge and the subsequent decrease. Similar flow characteristics can also be seen on the lower surface. The sharp leading edge
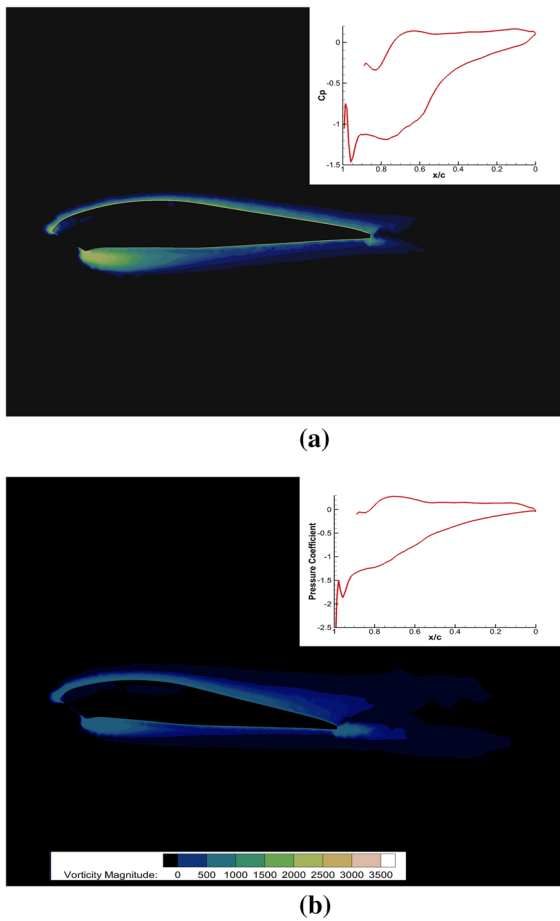
(a)

(b)

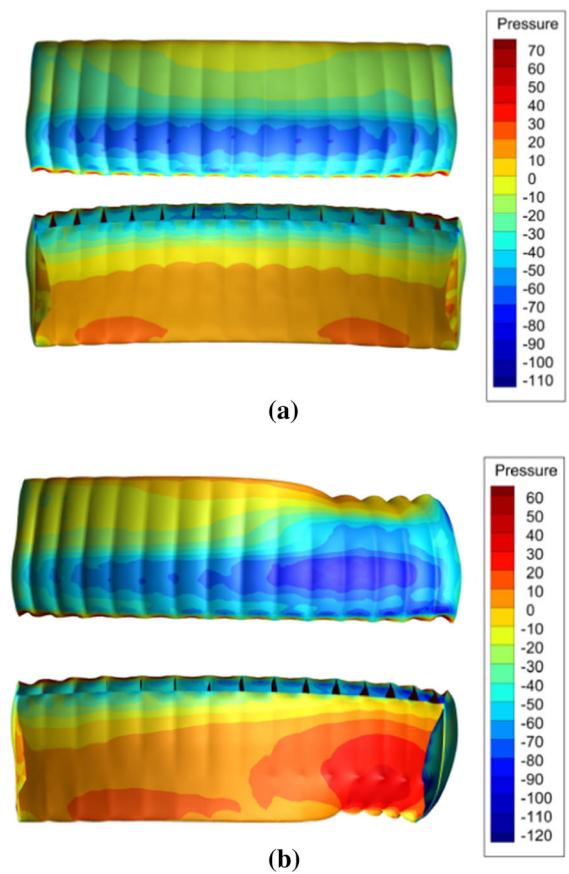**Fig. 15** Vorticity magnitude at **a** $\alpha = 8°$ and **b** $\alpha = 12°$

(a)

(b)

Fig. 16 Deformation and pressure distribution of parafoil canopy when **a** inflated and **b** left TE deflection

causes a high vortex area, which is due to the local pressure disturbance caused by the fluid being redirected by the inlet face and merging with the rest of the airflow at the corner. From the Cp curves, it can be found that there are two obvious peaks of negative pressure, which appear at the leading edge regions of the upper and lower surfaces respectively, corresponding to separated flow resulted from the acceleration of the airflow flowing through the inlet and the corners of the parafoil.

The above analysis proves that the method used in this paper can make the analysis of parafoil more reliable by solving the calculation problems related to the accurate representation of the canopy geometry and the involved complex multi-scale flow behaviors.

4.4 Influence of trailing edge deflection

When the parafoil system performs long-distance airdrop operations, it is expected to achieve an accurate and safe landing which requires eliminating lateral errors continuously according to the information of position, wind, and mission. Consequently, turning control is important during the process. The turning motion activated by TE deflecting causes further changes in the canopy shape and results in great changes in the surrounding flow field. In this section, we mainly analyze the aerodynamic characteristics of the parafoil in turning motion by FSI simulations.

The calculation time was primarily consumed in the process of canopy deforming as the pulling down of the control line which involving large displacements. Subsequent computations regarding the modification of angles of attack were less time-consuming. Figure 16

shows the predicted deformation results and pressure distribution of the parafoil canopy during the straight flight ($\delta = 0$) and left turn ($\delta = 40\%$) regimes. In the case of unilateral TE deflection, the pressure distributions on the canopy surfaces are no longer symmetrical, and the low-pressure area on the upper surface and the high-pressure area on the lower surface increase obviously at the same time. This indicates that the lift on the left side rises, which will result in a positive roll angle and may lead to the parafoil tilting outward.

Figure 17 depicts change curves of the lift coefficient, drag coefficients, and lift to drag ratio (L/D) within the full variety of unilateral TE deflections. It can be seen from Fig. 17a that the lift and drag coefficients approximately linearly increase until reaching the stall angle of attack. The TE deflection leads to the increase of lift coefficient up to stall, maximum lift coefficient, and drag coefficient in all angles of attack. However, as the angle of attack continues to grow until exceeding the stall angle of attack, the deviations of lift and drag coefficients with the TE deflection are not obvious. On the contrary, from Fig. 17b, the lift to drag ratio decreases with the TE deflection before stalling. After that, the discrepancies gradually decrease. The maximum L/D reduces from 5.55 to 4.81 with δ changing from 10% to 100%. These results indicate that the TE deflection has a negative effect on the parafoil aerodynamic performance.

4.5 Parameter identification results

From the aforementioned analysis, the aerodynamic characteristics of parafoil were studied considering the flexible deformations caused by inflating and different values of TE deflection. Next, a complete aerodynamic model can be built by identifying the unknown coefficients using the obtained data.

By substituting the aerodynamic data obtained from the FSI simulations into Eqs. (9)–(12), the aerodynamic parameters are identified and the results are shown in Table 5.

5 Dynamic simulation and validation

To verify that the six-DOF model established can accurately describe the flight performance of the parafoil system, we conducted simulation experiments.
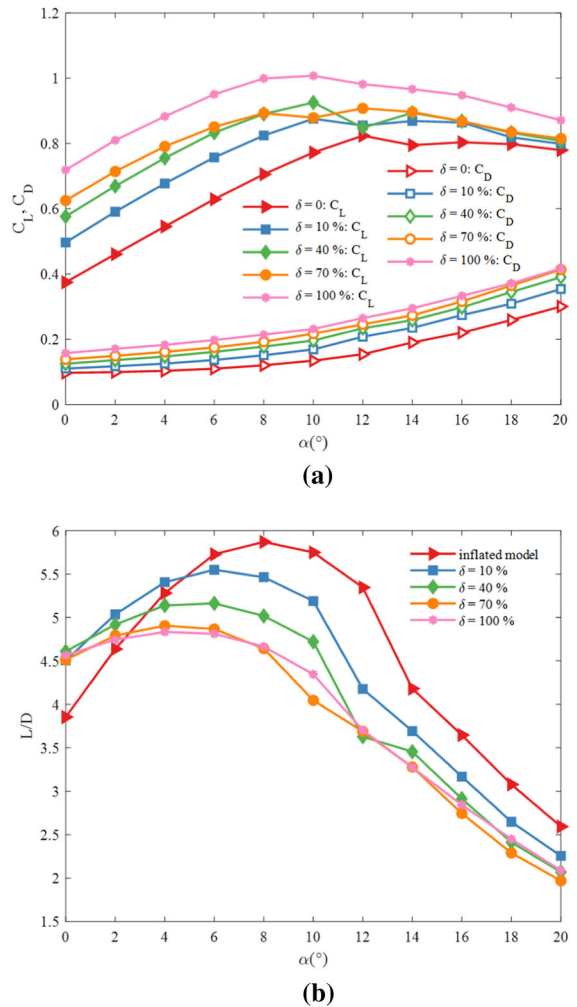

(a)

(b)

Fig. 17 Change curves of **a** lift and drag coefficients and **b** lift to drag ratio with the angles of attack for flexible parafoil model under different TE deflections

Table 5 Identification results of aerodynamic model factors

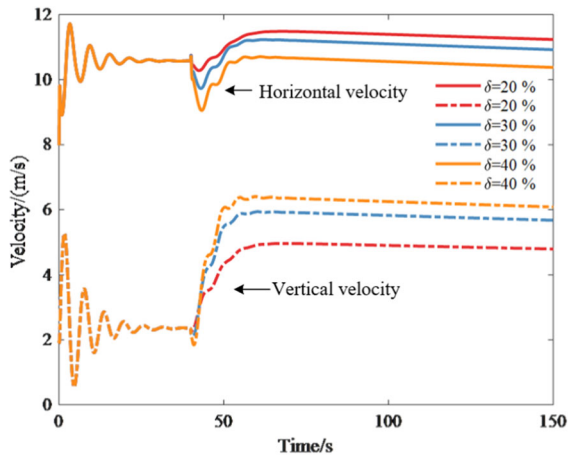| Variable	Value
C_{L0}	0.5885
$C_{L\alpha}$	0.8021
$C_{L\delta 0}$	0.2386
$C_{L\delta \alpha}$	0.0112
$C_{L\delta \alpha^2}$	-0.0083
C_{D0}	0.0505
$C_{D\alpha}$	0.7116
$C_{D\delta 0}$	0.1358
$C_{D\delta \alpha}$	-0.0887
$C_{D\delta \alpha^2}$	0.0026

Fig. 18 Change curves of velocities

5.1 Dynamic performance

Based on the established six-DOF model, the basic performances of the parafoil system were analyzed. The initial conditions of the simulation were set as follows: the initial horizontal speed was 7.5 m/s, the initial vertical speed was 2 m/s, and the initial Euler angles were all zero. The initial delivery height was 1000 m. The turning performance was mainly analyzed for the flight state of the parafoil system in the unilateral TE deflection. The values of TE deflection were set to 20%, 30%, and 40% respectively. The simulation time was 150 s, and the system started to turn at t=40 s when the influence of the initial state had been basically eliminated without considering the wind field.

Figure 18 shows the horizontal and vertical speeds of the parafoil system under different TE deflections. In the initial stage of gliding, oscillations occur at horizontal and vertical speeds. In actual flight, there are similar oscillations, which are caused by parafoil opening. The horizontal velocity instantly reduces to 10.28 m/s and 9.05 m/s when the left side is pulled down by 20% and 40%, respectively. The turning velocities are higher than the gliding period after the system reaches steady again. The steady gliding speed of the system is 10.57 m/s, and the stable horizontal velocities during turning are 11.34 m/s, 11.03 m/s and 10.47 m/s when $\delta = 20\%$, $\delta = 30\%$, $\delta = 40\%$, respectively. Therefore, the turning speed decreases with the unilateral deflection.

On contrary, the vertical velocity increases with the deflection, as shown in Fig. 18. The stable vertical velocities are 4.81 m/s, 5.69 m/s and 6.09 m/s corresponding to $\delta = 20\%$, $\delta = 30\%$, $\delta = 40\%$, respectively. This means that the height loss increases with the unilateral deflection.

Figure 19 shows the Euler angles of the parafoil system under different TE deflections. The yaw angle and roll angle are stable at 0 rad in the straight gliding stage. During the turning process, the yaw angle increases instantly and linearly. The rate of increase is positively related to deflections. In the initial gliding stage of the parafoil system, the pitch angle exhibits sinusoidal attenuation and oscillation and then stabilizes gradually. The initial pitch angle is about -0.08 rad (minus sign represents the direction) and increases suddenly during the turning phase. The oscillations become more obvious with the increase of the deflection. In the stable turning phase, the pitch angles increase by 0.22, 0.3, 0.34 (rad) when the TE deflections are 20%, 30%, and 40%, respectively. The changing trend of the roll angle is the same as the pitch angle and the yaw angle, increase by 0.78, 0.88, and 0.95 (rad) at 20%, 30%, and 40% deflections, respectively.

Figure 20 shows the horizontal trajectories of the system during flight. As the yaw angle is 0 rad at the steady gliding phase, the horizontal trajectory appears as a straight line. During the turning motion, the yaw angle increases linearly and the turning radius decreases with the yaw angle. The increase in roll angles in Fig. 19b cause the parafoil to tilt more severely in the spanwise direction, which is the main reason for the reduction of the turning radius and also an important factor affecting the stability of the parafoil.

Through the above simulations, the established flexible dynamic model can describe the actual behavior of the parafoil system in the steady gliding and turning phases. Through the analysis of the Euler angles, velocities, and trajectories, we can conclude that the change process basically accords with the actual motion law of a certain type of parafoil.

5.2 Trajectory tracking performance

Finally, we performed a simulation of tracking a straight path on the six-DOF model. The active disturbance rejection controller was adopted, and its specific design parameters can refer to [40]. The initial position was (0 m, 100 m, 600 m) and the target position was (1200 m, 1200 m, 0 m).
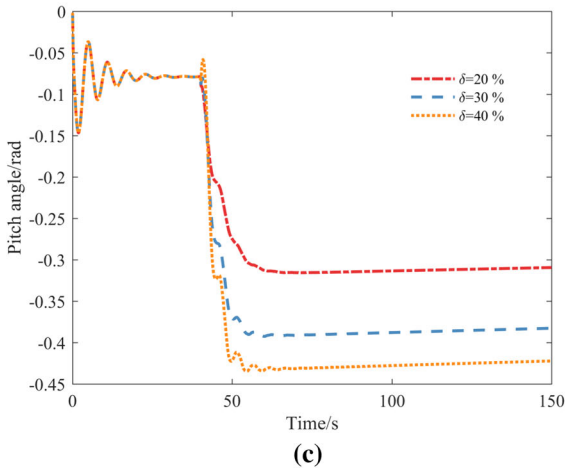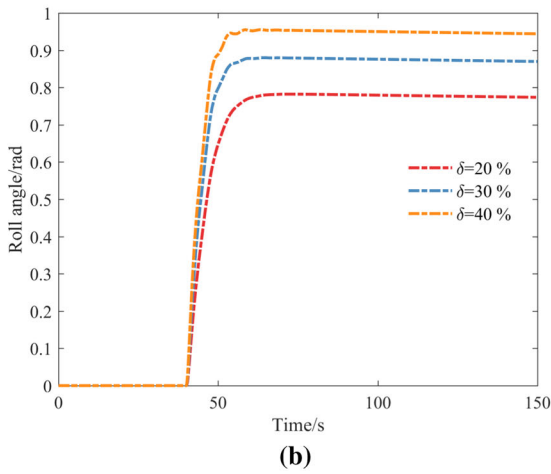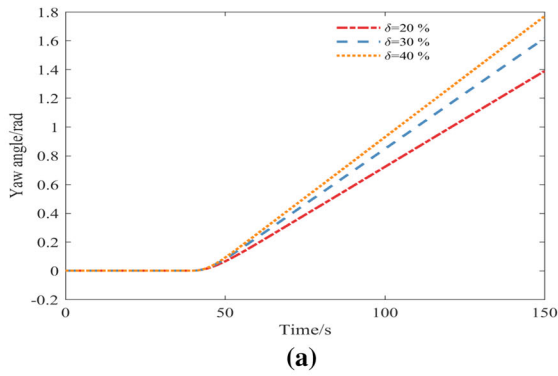
(a)

(b)

(c)

Fig. 19 Change curves of **a** yaw angle, **b** roll angle, and **c** pitch angle

Fig. 20 Trajectories in the horizontal plane

Fig. 21 Horizontal trajectory of tracking a straight line

Fig. 22 Change curves of velocities

Figure 21 indicates the tracking trajectory of the parafoil system in the horizontal plane. Under the action of the controller, the system quickly reaches the predetermined trajectory and moves toward the target
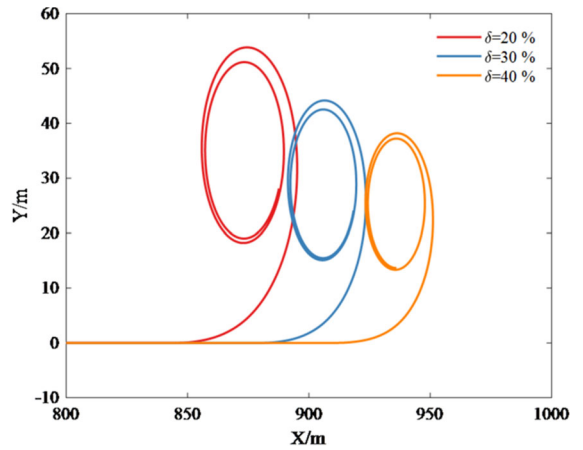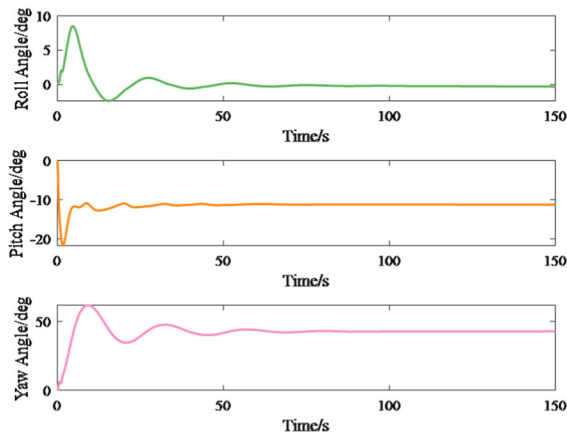
Fig. 23 Change curves of Euler angles

Table 6 Modal characteristics

Modes	Eigenvalues	Period (s)	Half-life time/time to double amplitude (s)
mode 1	$-0.74 \pm 4.32i$	1.454	0.936
mode 2	$-1.58 \pm 2.82i$	2.228	0.439
mode 3	-1.21	–	0.573
mode 4	-0.103	–	6.728

convergence. In addition, two real roots represent two monotonic modes, including fast convergence mode 3 and slow convergence mode 4.

5.4 Perturbation dynamics analysis

In the steady gliding state, the parafoil airdrop system needs to be stable with the oscillations of angular velocities remain small. Therefore, it is necessary to study the variations of the system states under gusts. The influence of gusts of 3 m/s and 6 m/s along the positive Y-axis at t = 50 s on the parafoil system were simulated respectively, and the action time of the wind field was 25 s.

Figure 24 illustrates the horizontal and vertical velocities of the parafoil system, which fluctuate under the action of gusts. The greater the wind speed, the more severe the fluctuations and amplitudes. The horizontal velocities reduce from 11.6 m/s to a minimum of 9 m/s and 5.8 m/s, respectively, at $v_f = 3$ m/s and $v_f = 6$ m/s. While the vertical velocities reduce by 0.6 m/s and 1.1 m/s, respectively. The instantaneous changes of horizontal velocities are relatively gentle under the action of wind fields, but become violent when the disturbance of wind fields disappear. And the vertical velocities show the same trends, but all velocities return to the original values eventually. Figure 25(a)–(c) illustrates the change of the Euler angles of the parafoil system under the interference of gusts. The oscillations become obvious with the increase of wind speed, but all angles can restore to stable states in the end.

6 Airdrop testing

Airdrop testing provides a quite effective means for validating the dynamic model of airdrop systems. The rigid body dynamic model of the parafoil system and
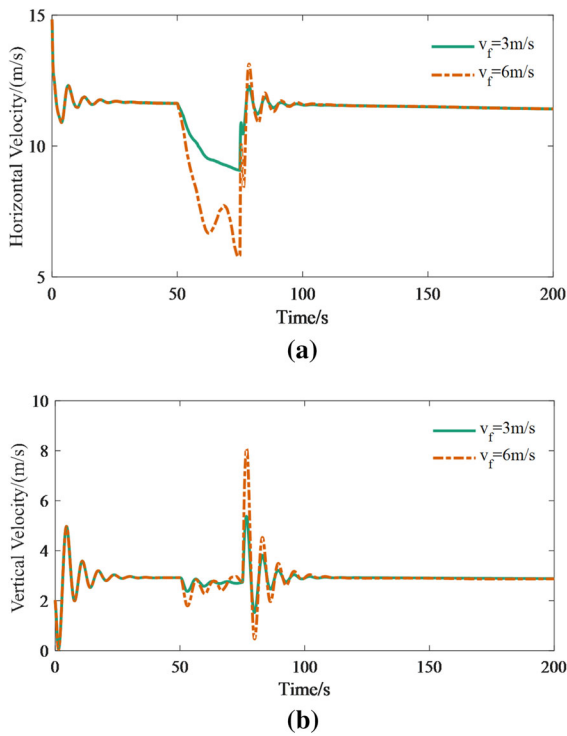
position. Figures 22 and 23 show the change curves of velocity and Euler angles in the process of tracking the target path. There are slight oscillations in the beginning, and then the system remains stable. The horizontal and vertical velocities stabilize at about 11.64 m/s and 3.87 m/s, respectively. And the Euler angles remain constant eventually after minor fluctuations.

From simulation results and analysis above, the parafoil system can accurately track the reference trajectory under control, which proves the reliability and feasibility of the dynamic model.

5.3 Stability analysis

To study the stability of the parafoil system at equilibrium states, we extracted the linear model from the established six-DOF nonlinear model, which is based on the small disturbance hypothesis at the equilibrium points of steady gliding, and analyzed the stability of the parafoil system using the developed linear system theory. An equilibrium state of the parafoil system in steady gliding was chosen with a horizontal velocity of 12 m/s, a vertical velocity of 2 m/s at an altitude of 1000 m, and a pitch angle of $-21.4°$, and then the linear system matrix was extracted and the corresponding eigenvalues were calculated. The results are shown in Table 6.

The negative real parts of the six eigenvalues prove the stability of the system. The linear system has two pairs of complex roots combined corresponding to two modes. Mode 2 has a longer period and slower convergence, while mode 1 has a shorter period and faster convergence.

Fig. 24 Change curves of **a** horizontal velocities, and **b** vertical velocities

the flexible dynamic model established in this paper are simulated and compared with the airdrop test to verify the improvement of the flexible dynamic model. Our research group conducted a flight test on the turning performance of the parafoil with geometric parameters given in Table 1. The altitude of the experiment site was 90 m, the height of the release point was 403 m. The turning spiral motion started from 250 m high, and the left steering line was retracted by 40%.

Figure 26 depicts the canopy deformations in the airdrop experiment and FSI coupling simulation under the constant control input on the left side. It can be seen from the figure that the unilateral pulling down of the control rope causes the canopy to bend about a quarter chordwise from the rear, and the simulation results show good similarity with the actual shapes of the canopy.

The position data were collected by the GPS module that fixed on the payload connecting to the parafoil through suspension ropes. The blue lines in Fig. 27 show the trajectories of the airdrop experiment. From the horizontal trajectories, the parafoil system gradually shifted under the influence of wind, and the wind
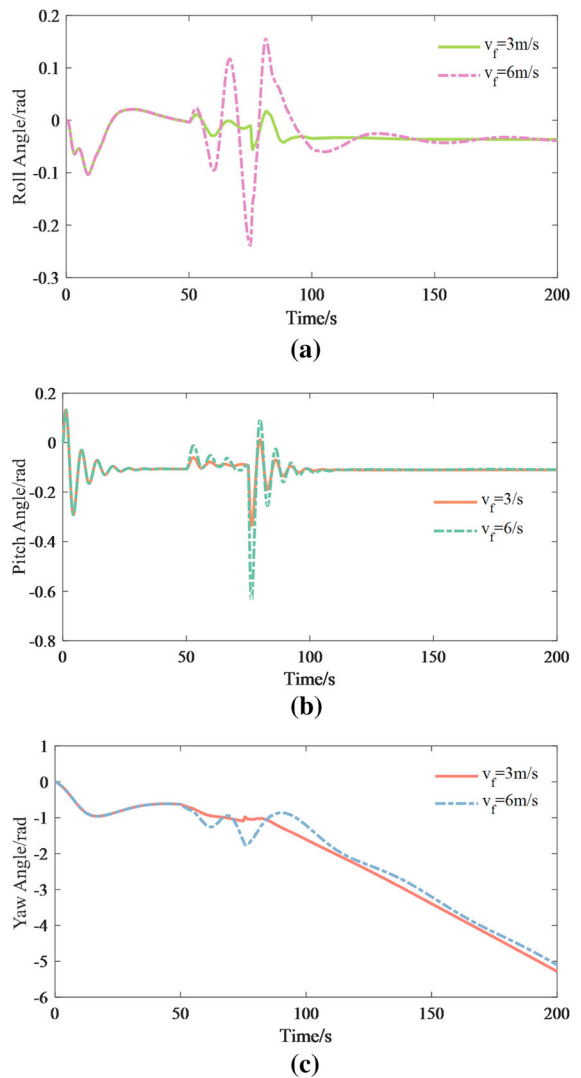

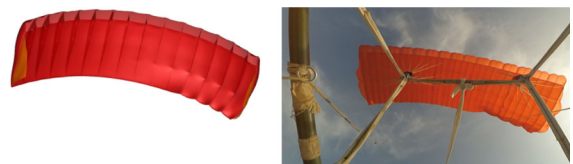**Fig. 25** Change curves of **a** roll angle, **b** pitch angle, and **c** yaw angle

Fig. 26 Comparison of the trailing edge deflection parafoil canopy between FSI simulation (left) and airdrop testing photo (right)

field varied with height. The wind information was extracted by the linear regression wind field identification method described in [41]. After filtering and pro-
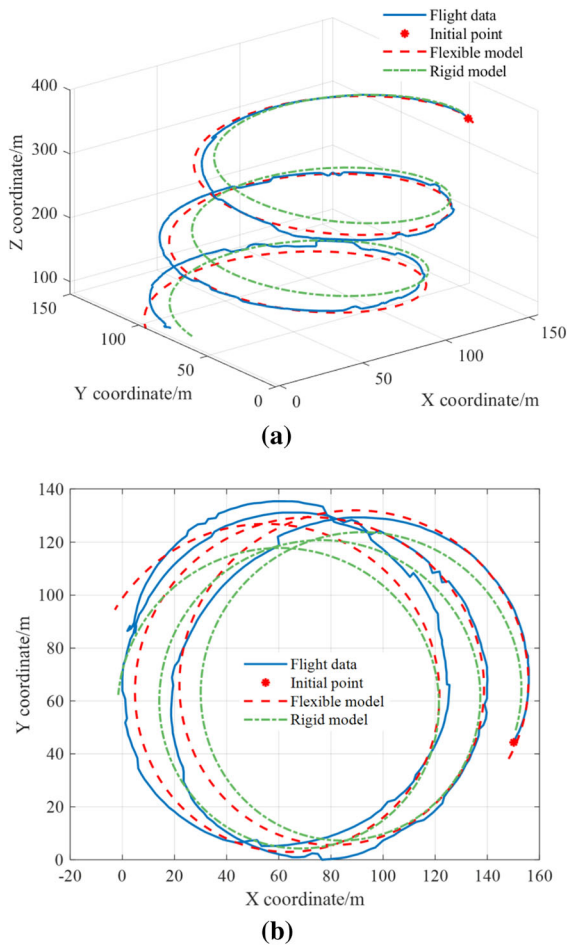
(a)

(b)

Fig. 27 Trajectories in **a** 3-D space and **b** horizontal plane

Fig. 28 Change curves of velocities

cessing the wind field information, the average speed of the wind field was 2 m/s and the direction is 160°. According to the above working conditions of turning motion in the airdrop testing, we carried out simulation experiments under the same conditions based on the established flexible dynamic model and rigid dynamic model.

From Figs. 12b, 27, and 28, the larger lift to drag ratio calculated by the flexible FSI model results in a larger horizontal velocity and a smaller vertical velocity compared to the rigid model. The airdrop test radius of the turning circle is about 58.4 m and the turning rate is approximately 10 m/s. The maximum deviations of the turning radius of the flexible model and rigid model from the airdrop testing data are 7.5 m and 14.9 m, respectively. Overall the turning radius of the flexible model is closer to the airdrop experimental data. From
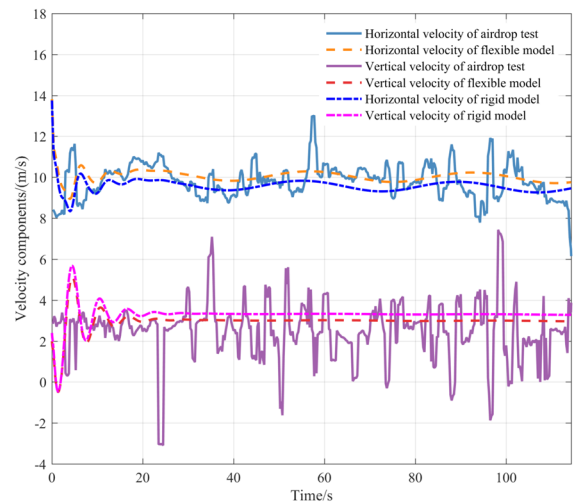
Fig. 27, we can see that the simulated trajectory by flexible model better coincides with the flight trajectory of the airdrop system.

The horizontal velocity fluctuates slightly under the influence of wind and the error is less than 1 m/s. The local error may be as a result of the wind field estimation error and complicated turbulence in the air. We know that the horizontal movement of the ambient flow has a greater effect than the vertical [42], so the error of the velocity in vertical is more slight than the horizontal. Moreover, the wind speed is small and the control quantity remains constant, which is why the vertical velocity is almost unchanged. From the above analysis, the aerodynamic model established by FSI coupling can accurately represent the characteristics of the actual parafoil system.

7 Conclusions

Advances in increasing the fidelity of the aerodynamic model of the parafoil system, contribute to modeling and simulation tools that are more precise to predict the maneuvering capability and verify the control algorithms. This study aims at establishing an accurate model of the parafoil system to reduce the distance between the dynamic simulation and actual flight tests.

The core of the operating performance of the parafoil system is the reaction to TE deflections due to the variation of interaction between the canopy material and ambient airflow. In this study, we used a strongly cou-

pled FSI method to estimate the aerodynamic forces acting on the parafoil under steady inflation and various TE deflections. Considering the intense interactions between the flexible canopy and surrounding flow field, both the deformation of the canopy and flow field characteristics were analyzed to get a better understanding of aerodynamic behaviors of the full-scale parafoil.

This study makes a step forward to connecting the flight dynamics simulation of parafoil and the high fidelity FSI method. The aerodynamic coefficients were identified using LRM and incorporated into a six-DOF dynamic model of the parafoil system. Simulation results validate the dynamic stability of the model and the feasibility of trajectory tracking. Finally, flight simulation results of the established flexible model and rigid model under turning motion were compared with airdrop testing data, which demonstrates that the proposed methods are more accurate to the application of predicting the actual behavior of parafoil systems.

Declarations

Conflict of interest The authors declare that they have no conflict of interest.

References

1. Bennett, T., Fox, R.: Design, Development & Flight Testing of the NASA X-38 7500 ft2 Parafoil Recovery System. In: 17th AIAA Aerodynamic Decelerator Systems Technology Conference and Seminar. American Institute of Aeronautics and Astronautics (2003)
2. Gorman, C.M., Slegers, N.J.: Modeling of Parafoil-Payload Relative Yawing Motion on Autonomous Parafoils. In: 21st AIAA Aerodynamic Decelerator Systems Technology Conference and Seminar. p. 2614. American Institute of Aeronautics and Astronautics (2011)
3. Yakimenko, O.A.: Precision Aerial Delivery Systems: Modeling, Dynamics, and Control. American Institute of Aeronautics and Astronautics, Inc. (2015)
4. Ghoreyshi, M., Bergeron, K., Jirásek, A., Seidel, J., Lofthouse, A.J., Cummings, R.M.: Computational aerodynamic modeling for flight dynamics simulation of ram-air parachutes. Aerosp. Sci. Technol. **54**, 286–301 (2016)
5. Goodrick, T.: Theoretical study of the longitudinal stability of high-performance gliding airdrop systems. In: 5th Aerodynamic Deceleration Systems Conference. pp. 1–9. American Institute of Aeronautics and Astronautics, Albuquerque, NM, U.S.A. (1975)
6. Jann, T.: Aerodynamic model identification and GNC design for the parafoil-load system ALEX. In: 16th AIAA Aerodynamic Decelerator Systems Technology Conference and Seminar. American Institute of Aeronautics and Astronautics, Boston, MA, U.S.A. (2001)
7. Slegers, N., Gorman, C.: Comparison and Analysis of Multibody Parafoil Models With Varying Degrees of Freedom. In: 21st AIAA Aerodynamic Decelerator Systems Technology Conference and Seminar. American Institute of Aeronautics and Astronautics (2011)
8. Zhu, E., Sun, Q., Tan, P., Chen, Z., Kang, X., He, Y.: Modeling of powered parafoil based on Kirchhoff motion equation. Nonlinear Dyn. **79**, 617–629 (2015)
9. Devalla, V., Jaiswal, R., Mondal, A.K., Sharma, K.K., Thomas, C., Prakash, O.: Estimation of Lateral Directional Aerodynamic Derivatives from Flight Data of Unmanned Powered Parafoil Aerial Vehicle. In: 2018 Atmospheric Flight Mechanics Conference. American Institute of Aeronautics and Astronautics, Atlanta, Georgia (2018)
10. Ghoreyshi, M., Bergeron, K., Seidel, J., Jirásek, A., Lofthouse, A.J., Cummings, R.M.: Prediction of aerodynamic characteristics of Ram-Air parachutes. J. Aircr. **53**, 1802–1820 (2016)
11. Wu, W., Sun, Q., Luo, S., Sun, M., Chen, Z., Sun, H.: Accurate calculation of aerodynamic coefficients of parafoil airdrop system based on computational fluid dynamic. Int. J. Adv. Robot. Syst. **15**, 1–16 (2018)
12. Tao, J., Sun, Q., Liang, W., Chen, Z., He, Y., Dehmer, M.: Computational fluid dynamics based dynamic modeling of parafoil system. Appl. Math. Model. **54**, 136–150 (2018)
13. Zhu, H., Sun, Q., Wu, W., Sun, M., Chen, Z.: Accurate modeling and control for parawing unmanned aerial vehicle. Acta Aeronaut. Astronaut. Sin. **40**, 79–91 (2019). (**(in Chinese)**)
14. Potvin, J., Bergeron, K., Brown, G., Charles, R., Desabrais, K., Johari, H., Kumar, V., McQuilling, M., Morris, A., Noetscher, G., Tutt, B.: The Road Ahead: A White Paper on the Development, Testing and Use of Advanced Numerical Modeling for Aerodynamic Decelerator Systems Design and Analysis. In: 21st AIAA Aerodynamic Decelerator Systems Technology Conference and Seminar. p. 2501 (2011)
15. Vassen, J.-M., DeVincenzo, P., Hirsch, C., Leonard, B.: Strong Coupling Algorithm To Solve Fluid-Structure-Interaction Problems With A Staggered Approach. In: 7th European Symposium on Aerothermodynamics. p. 128, Brugge, Belgium (2011)
16. Benney, R.J., Stein, K., Kalro, V., Tezduyar, T., Leonard, J.W., Accorsi, M.L.: Parachute Performance Simulations: A 3D Fluid-Structure Interaction Model. In: Proceedings of 21st Army Science Conference, Norfolk, Virginia (1998)
17. Nie, S., Cao, Y., Wu, Z.: Numerical simulation of parafoil inflation via a Robin-Neumann transmission-based approach. Proc. Inst. Mech. Eng. Part G J. Aerosp. Eng. **232**, 797–810 (2018)
18. Burnett, B.: Coupled Fluid-Structure Interaction Modeling of a Parafoil, Embry-Riddle Aeronautical University (2016)
19. Altmann, H.: Fluid-Structure Interaction Analysis of Ram-Air Parafoil Wings. In: 23rd AIAA Aerodynamic Decelera-

tor Systems Technology Conference. American Institute of Aeronautics and Astronautics, Daytona Beach, FL (2015)

20. Fogell, N.A., Sherwin, S., Cotter, C.J., Iannucci, L., Palacios, R., Pope, D.J.: Fluid-structure interaction simulation of the inflated shape of ram-air parachutes. In: AIAA Aerodynamic Decelerator Systems (ADS) Conference. p. 1326. American Institute of Aeronautics and Astronautics, Daytona Beach, Florida (2013)

21. Fogell, N.A., Iannucci, L., Bergeron, K.: Fluid-Structure Interaction Simulation study of a Semi-Rigid Ram-Air Parachute Model. In: 24th AIAA Aerodynamic Decelerator Systems Technology Conference. p. 3547. American Institute of Aeronautics and Astronautics, Denver, Colorado (2017)

22. Zhang, C., Cao, Y.: Numerical simulation of parafoil aerodynamics and structural deformation based on loose coupled method. J. Beijing Univ. Aeronaut. Astronaut. **39**, 605–609 (2013). (**(in Chinese)**)

23. Takizawa, K., Tezduyar, T.E., Terahara, T.: Ram-air parachute structural and fluid mechanics computations with the Space-Time Isogeometric Analysis (ST-IGA). Comput. Fluids **141**, 191–200 (2016)

24. Charles, R.D.: Simulation of the Baseline Performance Characteristics of a Ram-Air Parachute. In: 24th AIAA Aerodynamic Decelerator Systems Technology Conference. American Institute of Aeronautics and Astronautics, Denver, Colorado (2017)

25. Gao, X.: Assessment of Simulating Underwater Impact Using the ICFD Slover in LS-DYNA. Memorial University of Newfoundland, Canada (2016)

26. Pin, F. Del, Software, L., Corporation, T.: LS-DYNA ® R7: Strong Fluid Structure Interaction (FSI) capabilities and associated meshing tools for the incompressible CFD solver (ICFD), applications and examples. In: 9th European LS-DYNA Conference (2013)

27. Garrec, M. Le, Seulin, M., Lapoujade, V.: Airdrop Sequence Simulation using LS-DYNA ICFD Solver and FSI Coupling. In: 15th International LS-DYNA users Conference. , Detroit, MI, USA. (2018)

28. Garrec, M.L.E., Poncet, A., Lapoujade, V.: Parachute deployment simulations using LS-DYNA ICFD solver and strong FSI coupling. In: 12th European LS-DYNA Conference, Koblenz, Germany (2019)

29. Barrows, T.M.: Apparent Mass of Parafoils with Spanwise Camber. J. Aircr. **39**, 445–451 (2002)

30. Ward, M.: Adaptive glide slope control for parafoil and payload aircraft, (2012)

31. Wu, W., Sun, Q., Sun, M., Dehmer, M., Chen, Z.: Modeling and control of parafoils based on computational fluid dynamics. Appl. Math. Model. **70**, 378–401 (2019)

32. Eslambolchi, A., Johari, H.: Simulation of flowfield around a ram-air personnel parachute canopy. J. Aircr. **50**, 1628–1636 (2013)

33. Mohammadi, M.A., Johari, H.: Computation of flow over a high-performance parafoil canopy. J. Aircr. **47**, 1338–1345 (2010)

34. Spalart, P., Allmaras, S.: A One-Equation Turbulence Model for Aerodynamic Flows. In: 30th Aerospace Sciences Meeting and Exhibit, Reno,NV,U.S.A. (1992)

35. Gal-Chen, T., Somerville, R.C.J.: Numerical solution of the navier-stokes. J. Comput. Phys. **17**, 276–310 (1975)

36. Caldichoury, I., Paz, R.R., Facundo Del Pin: ICFD theory manual incompressible fluid solver in LS-DYNA. Livermore Software Technology Corporation (2014)

37. Nicolaides, J.: Parafoil wind tunnel tests. Notre Dame Univ in Dept of Aerospace and Mechanical Engineering (1971)

38. Cao, Y., Zhu, X.: Effects of characteristic geometric parameters on parafoil lift and drag. Aircr. Eng. Aerosp. Technol. **85**, 280–292 (2013)

39. Wang, L.: The theory and application of parachutes, 570–571. China Astronautic Publishing House, Beijing (1997)

40. Tao, J., Sun, Q., Tan, P., Chen, Z., He, Y.: Active disturbance rejection control (ADRC)-based autonomous homing control of powered parafoils. Nonlinear Dyn. **86**, 1461–1476 (2016)

41. Gao, H., Tao, J., Dehmer, M., Emmert-Streib, F., Sun, Q., Chen, Z., Xie, G., Zhou, Q.: In-flight wind field identification and prediction of parafoil systems. Appl. Sci. **10**(6), 1958 (2020)

42. Sun, H., Sun, Q., Wu, W., Chen, Z., Tao, J.: Altitude control for flexible wing unmanned aerial vehicle based on active disturbance rejection control and feedforward compensation. Int. J. Robust Nonlinear Control **30**, 222–245 (2020)